nature energy

Article

https://doi.org/10.1038/s41560-024-01487-w

Ion-induced field screening as a dominant factor in perovskite solar cell operational stability

In the format provided by the authors and unedited

Supplementary Materials Table-of-Content

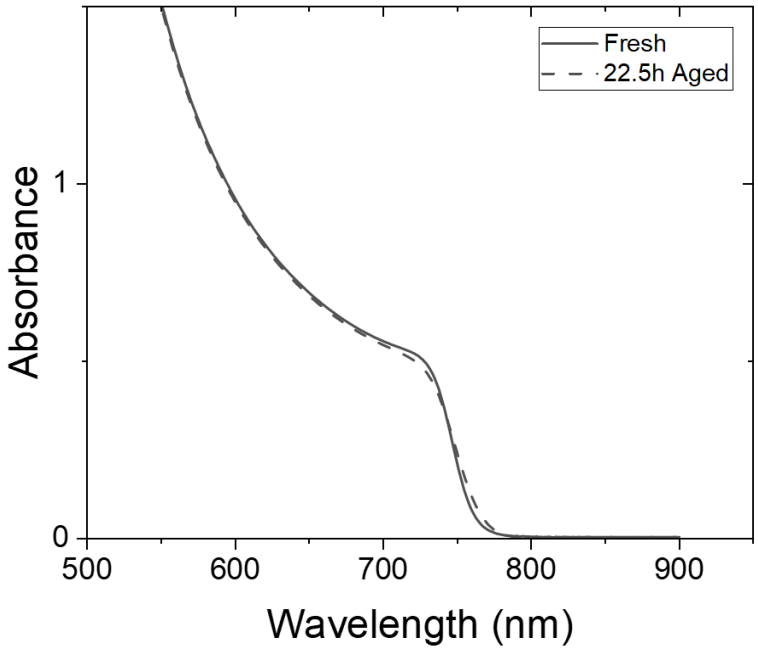

Supplementary Figure 1. Absorption spectroscopy of fresh and degraded triple cation films after 22.5 h of illumination with a 1 sun equivalent LED in N_2.

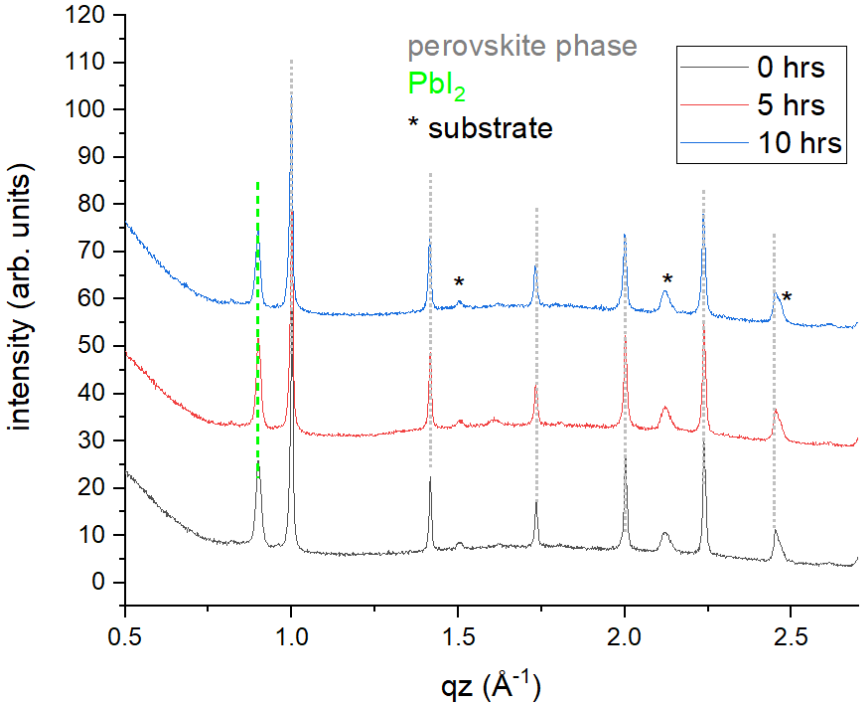

Supplementary Figure 2. X-ray diffraction measurements of fresh and degraded triple cation films after different hours of illumination revealed no apparent change during the illumination within the first hours of degradation.

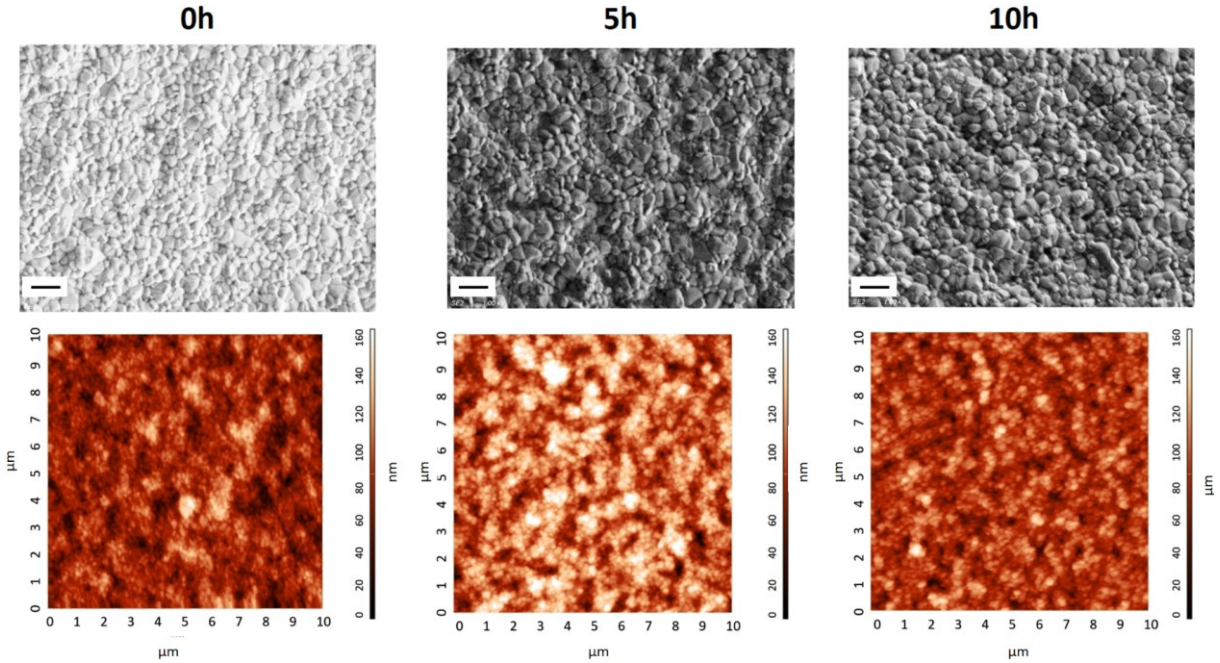

Supplementary Figure 3. SEM and AFM of fresh and degraded triple cation films after different hours of illumination. The scale bar of the SEM images is 500 nm.

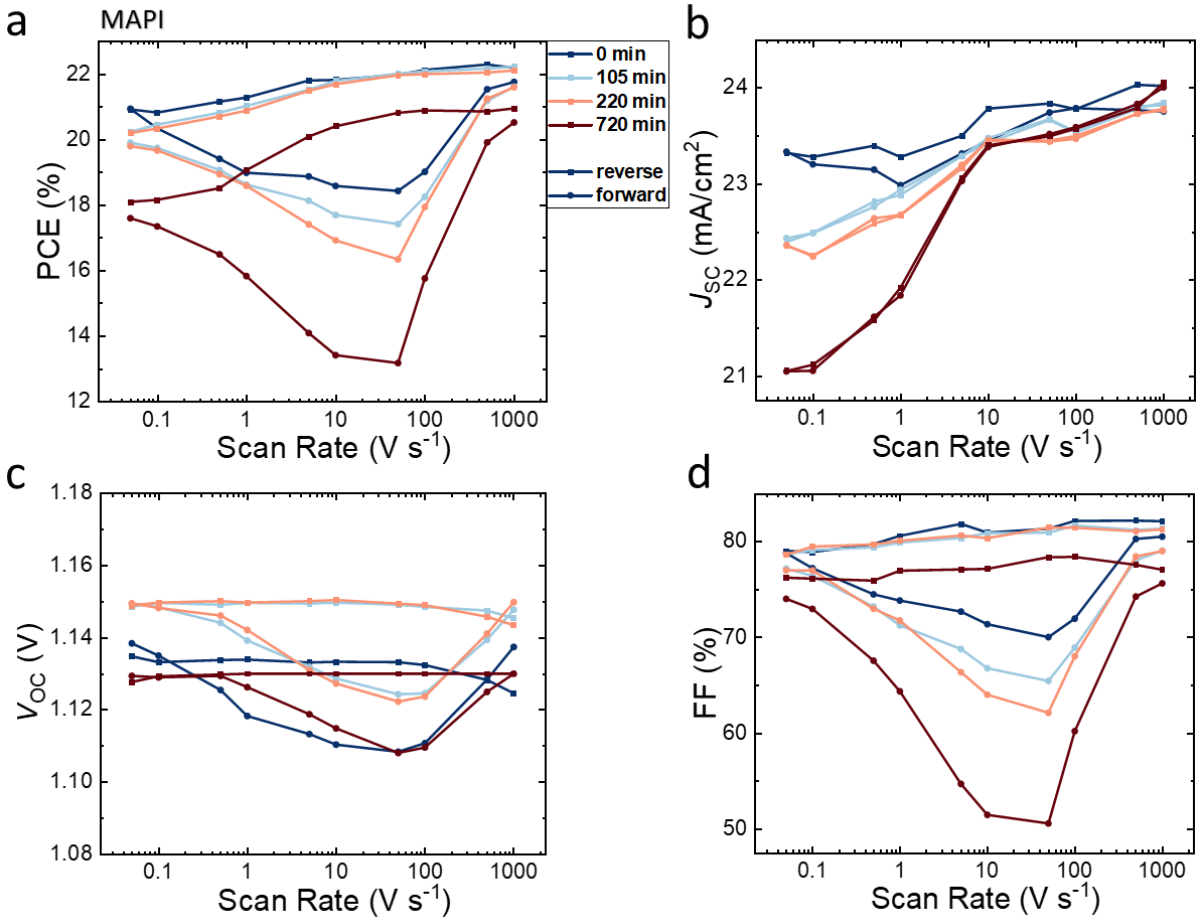

Supplementary Figure 4. a The power conversion efficiency (PCE), **b** short-circuit current density (J_{SC}), **c** open-circuit voltage (V_{OC}), and **d** fill factor (FF) from current-voltage characteristics measured at different scan speeds for $MAPbI_3$ perovskite solar cells after different ageing times.

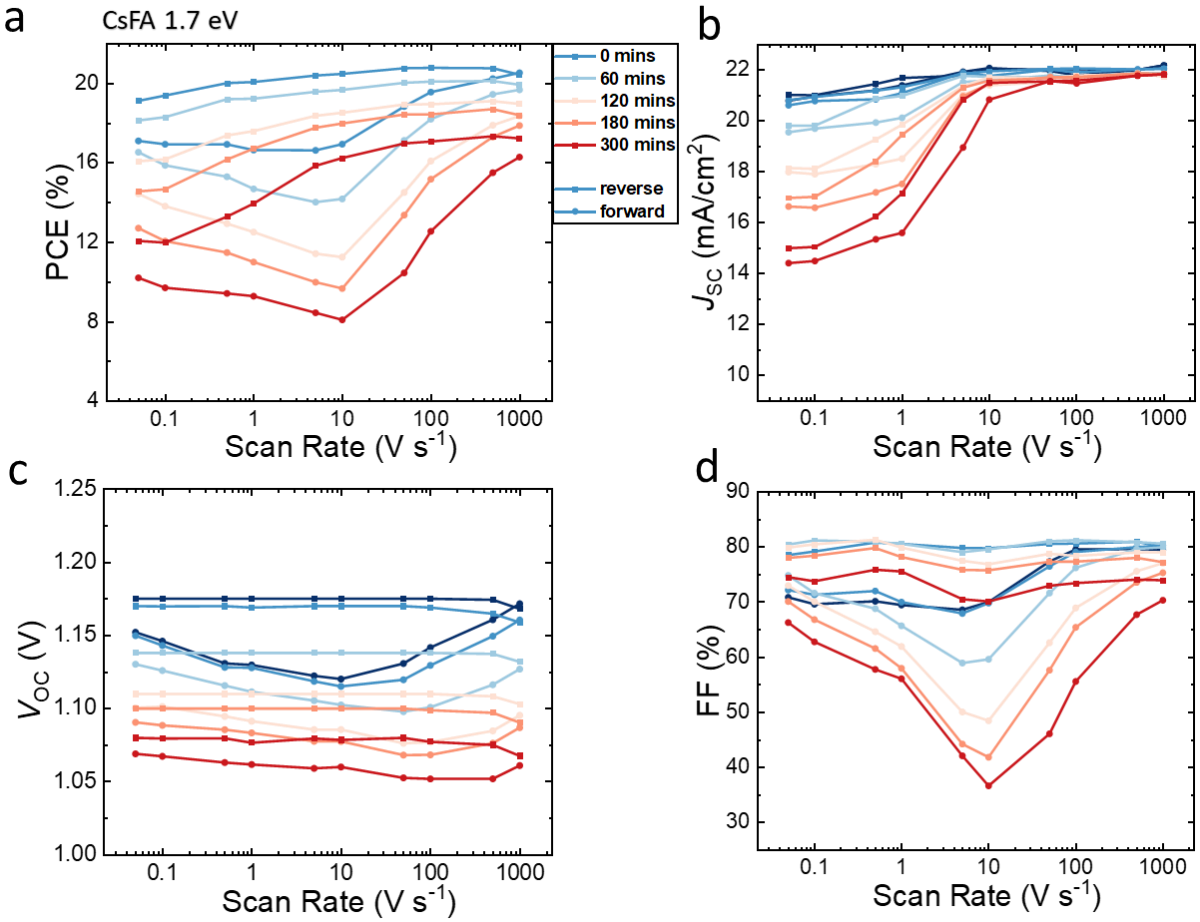

Supplementary Figure 5. a The power conversion efficiency (PCE), **b** short-circuit current density (J_{SC}), **c** open-circuit voltage (V_{OC}), and **d** fill factor (FF) from current-voltage characteristics measured at different scan speeds for $FA_{0.85}Cs_{0.15}Pb(I_{0.77}Br_{0.23})_3$ perovskite solar cells after different ageing times.

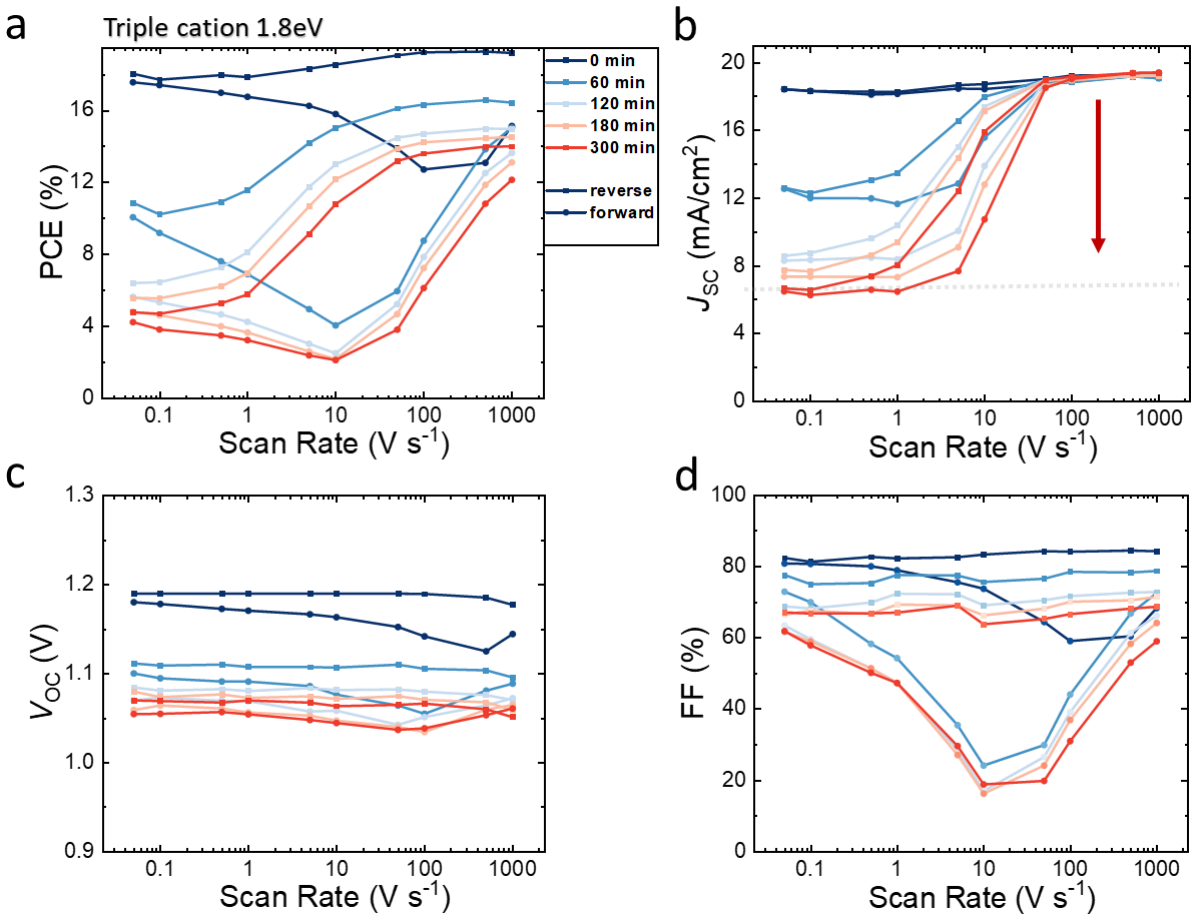

Supplementary Figure 6. a The power conversion efficiency (PCE), **b** short-circuit current density (J_{SC}), **c** open-circuit voltage (V_{OC}), and **d** fill factor (FF) from current-voltage characteristics measured at different scan speeds for 1.8eV wide gap $Cs_{0.05}(FA_{0.60}MA_{0.40})_{0.95}Pb(I_{0.60}Br_{0.40})_3$ perovskite solar cells after different ageing times.

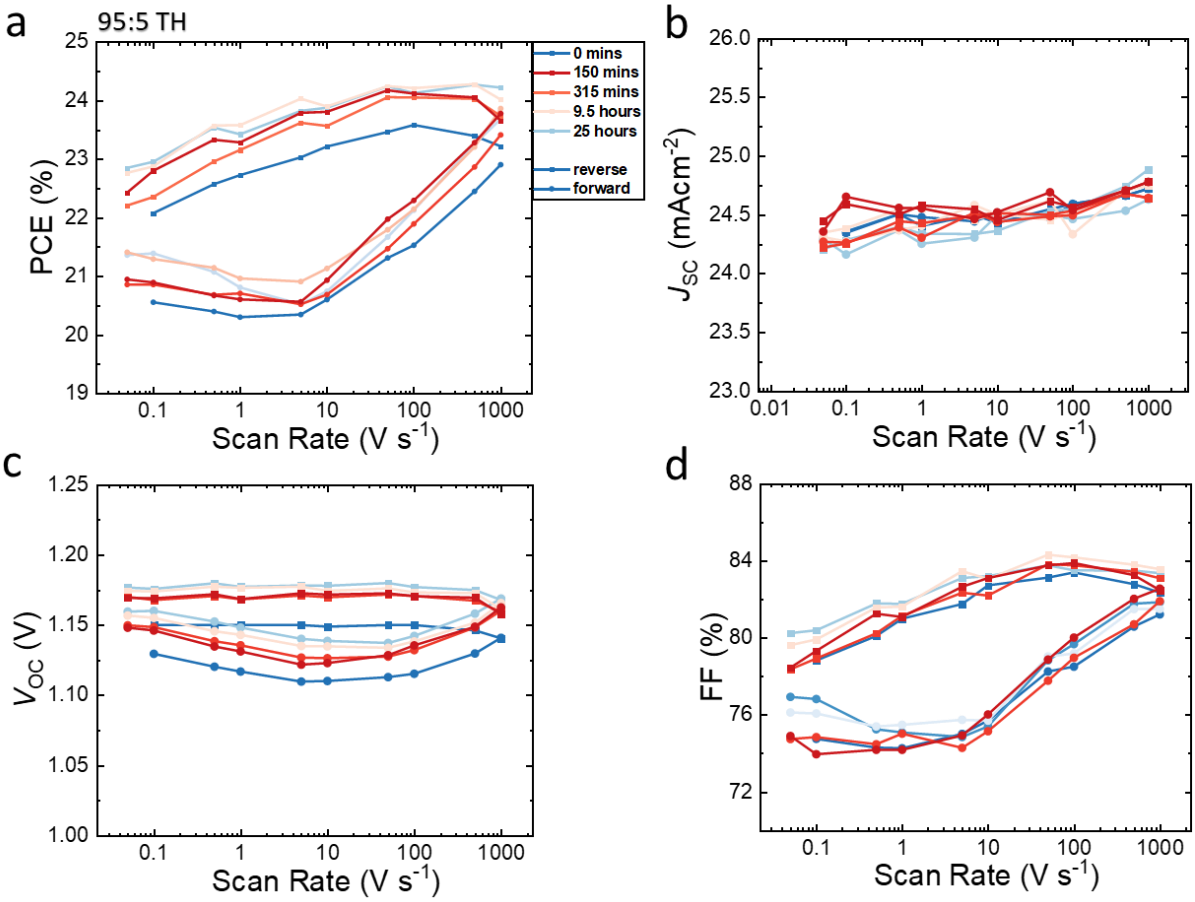

Supplementary Figure 7. a The power conversion efficiency (PCE), **b** short-circuit current density (J_{SC}), **c** open-circuit voltage (V_{OC}), and **d** fill factor (FF) from current-voltage characteristics measured at different scan speeds for 95:5 triple halide ($Cs_{0.05}(FA_{0.95}MA_{0.05})_{0.95}Pb(I_{0.95}Br_{0.05})_3$ + 20 mol% MACl) perovskite solar cells after different ageing times.

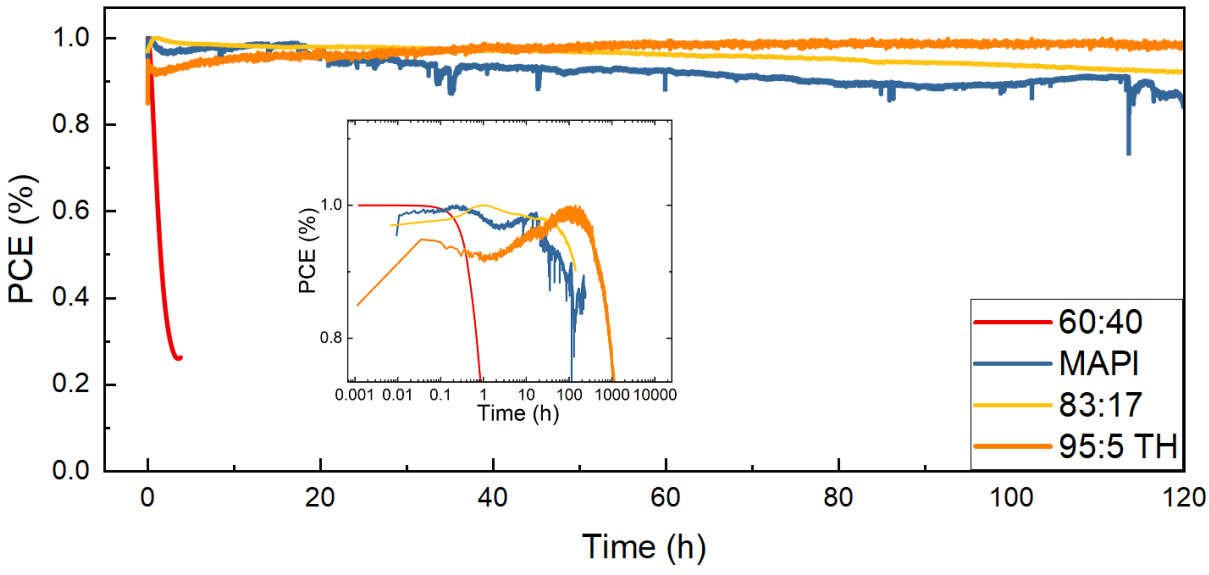

Supplementary Figure 8. Maximum power point tracking of the devices presented in the manuscript. The initial/normalized PCE is 17%/17% for the 60:40 cell, 16.15%/16.62% for the MAPI cell, 19%/19.60% for the triple cation cell, and 20.13%/23.70% for the 95:5 TH cell.

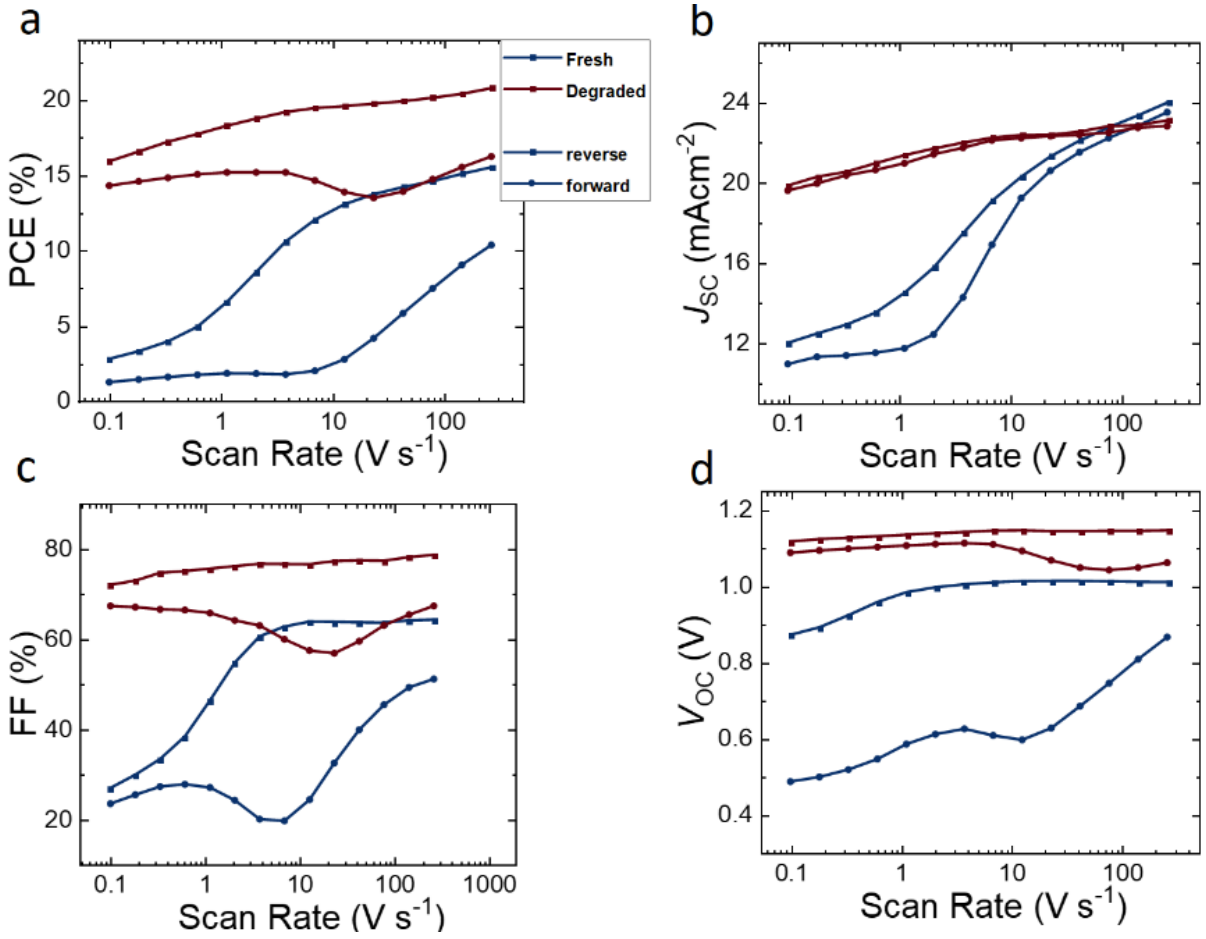

Supplementary Figure 9. The power conversion efficiency (PCE), **b** short-circuit current density (J_{SC}), **c** open-circuit voltage (V_{OC}), and **d** fill factor (FF) from current-voltage characteristics measured at different scan speeds for *nip*-type $(FAPbI3)_{0.99}(CsPbBr3)_{0.01}$:35mol% MACl perovskite solar cells after different ageing times.

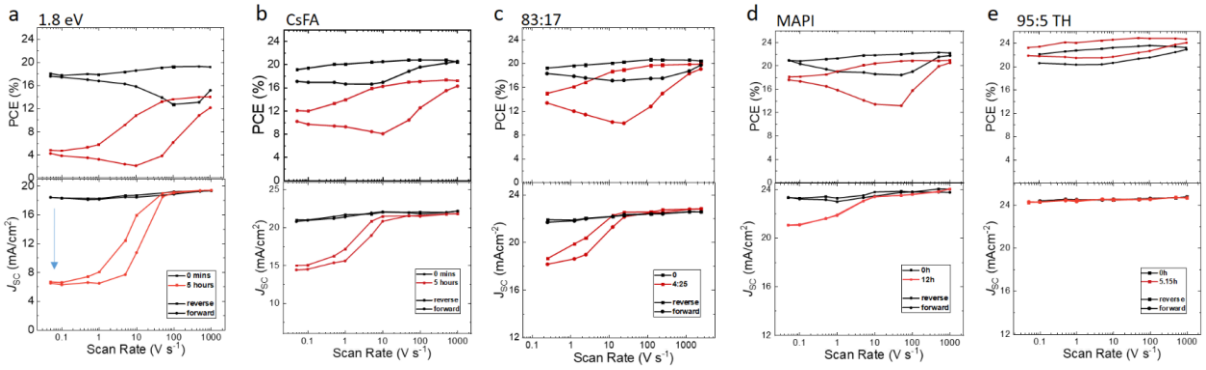

Supplementary Figure 10. a The power conversion efficiency (PCE), **b** short-circuit current density (J_{SC}) measured at different scan speeds for different perovskite systems before and after 5h of illumination (12h in case of MAPI).

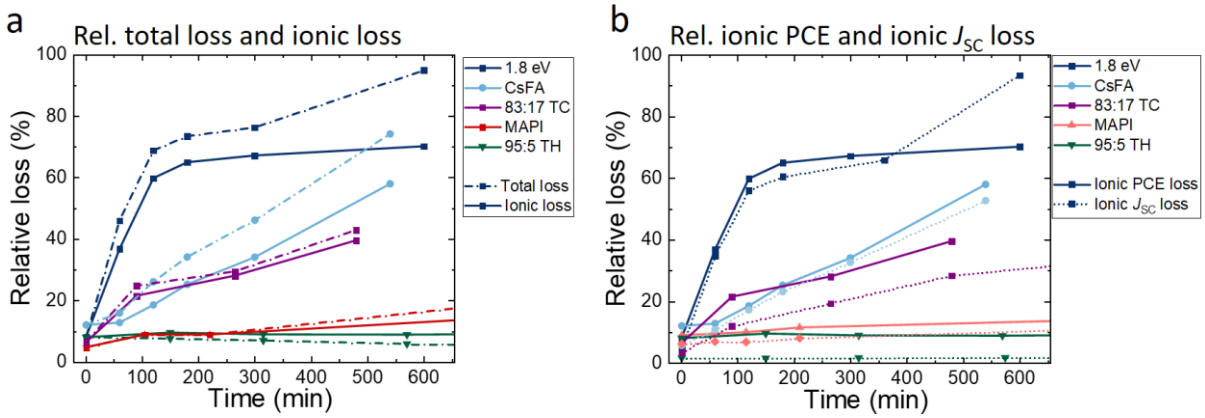

Supplementary Figure 11. a Relative total loss ($1\text{-}PCE_{slow}/PCE_{fast,initial}$) and ionic loss ($1\text{-}PCE_{slow}/PCE_{fast}$) and **b** relative ionic PCE ($1\text{-}PCE_{slow}/PCE_{fast}$) versus ionic *J*sc loss ($1\text{-}J_{SC,slow}/J_{SC,fast}$) for various systems.

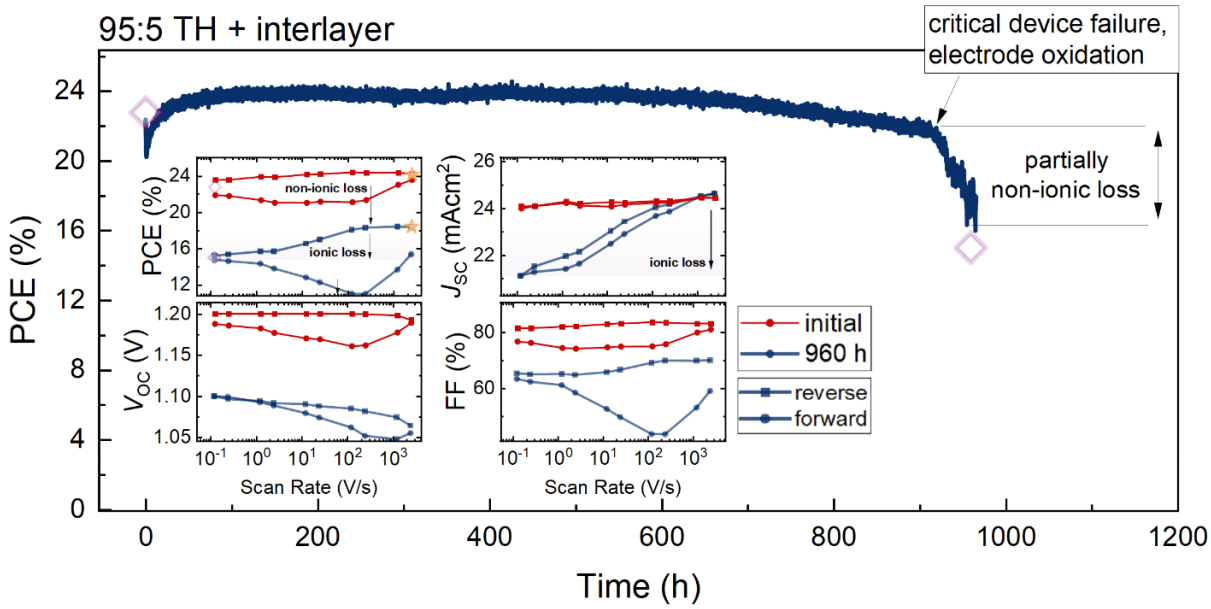

Supplementary Figure 12. Maximum point tracking of interlayer-modified $Cs_{0.05}(FA_{0.95}MA_{0.05})_{0.95}Pb(I_{0.95}Br_{0.05})_3$ + 20 wt% MACl ("95:5 TH"). Substantial non-ionic losses appear due to a sudden critical device failure (oxidation of the electrode visible by the eye). Nevertheless, enhanced ionic losses are still present in these devices as visible from the reduction of the short-circuit current contributing to approximately 37.4% of the total degradation loss observed.

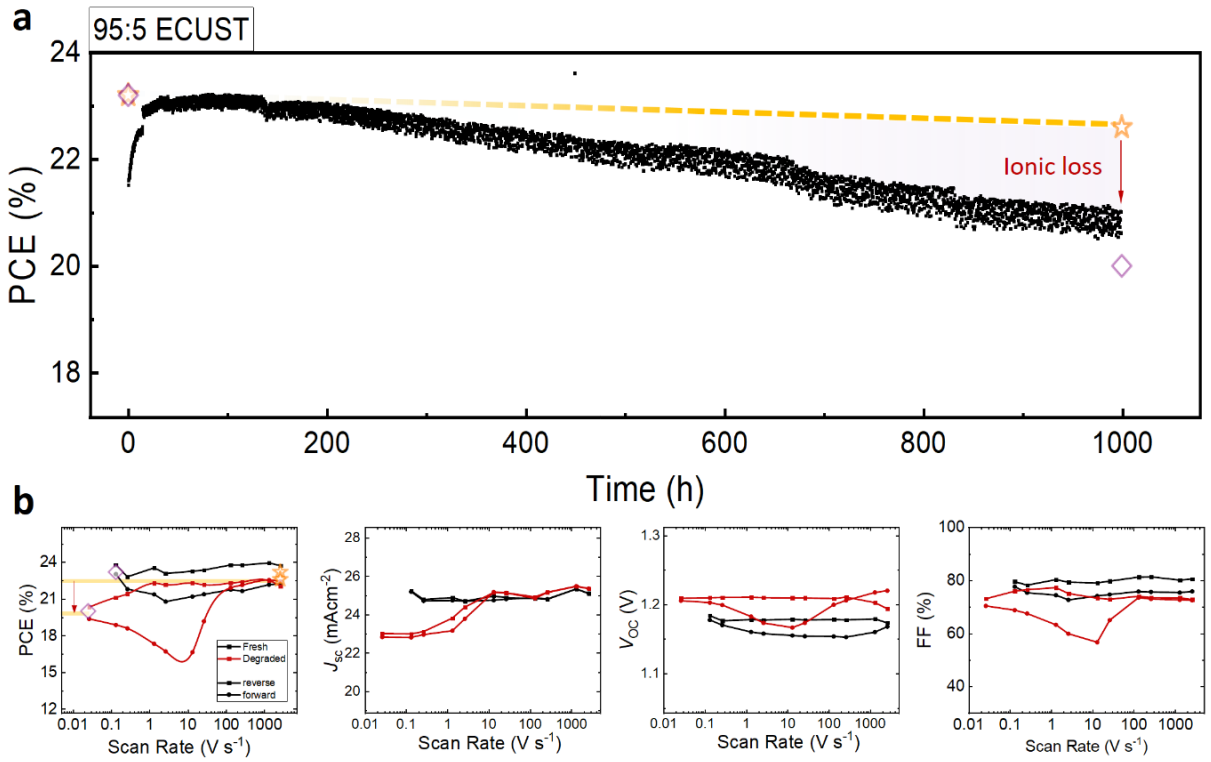

Supplementary Figure 13. **a** Maximum power point (MPP) tracking of *pin*-type cells made from $Cs_{0.05}(FA_{0.98}MA_{0.02})_{0.95}Pb(I_{0.98}Br_{0.02})_3$ ("98:2") and $Cs_{0.05}(FA_{0.95}MA_{0.05})_{0.95}Pb(I_{0.95}Br_{0.05})_3$ ("95:5 ECUST"), respectively, demonstrating that the degradation loss is also largely ionic. **b** Power conversion efficiency (PCE), current density (J_{SC}), open-circuit voltage (V_{OC}), fill factor (FF) of $Cs_{0.05}(FA_{0.95}MA_{0.05})_{0.95}Pb(I_{0.95}Br_{0.05})_3$ "95:5 ECUST" cells at different scan speeds in reverse and forward scan directions for different ageing times. The steady-state and ion-freeze PCE are marked in panels a,b by the diamonds and stars, respectively, while the red arrows and the shading highlight the ionic losses in panel a.

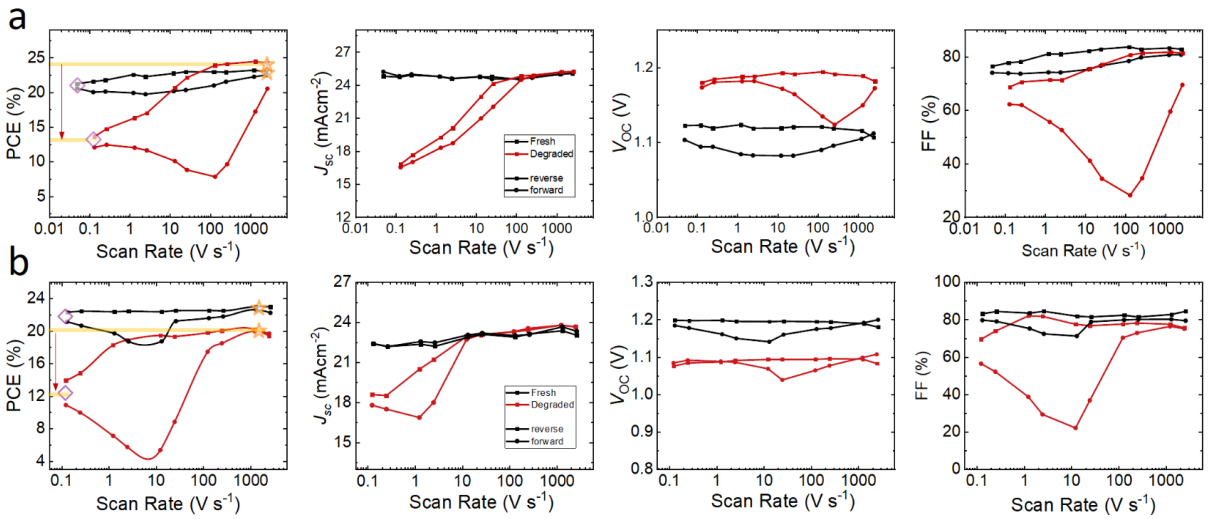

Supplementary Figure 14. **a** Power conversion efficiency (PCE), current-density (J_{SC}), open-circuit voltage (V_{OC}), fill factor (FF) of $Cs_{0.05}(FA_{0.95}MA_{0.05})_{0.95}Pb(I_{0.95}Br_{0.05})_3$ "95:5 TH" cells at different scan speeds in reverse and forward scan directions for after different ageing times corresponding to Figure 4a in the main text. **b** PCE, J_{SC}, V_{OC}, and FF of $Cs_{0.05}(FA_{0.98}MA_{0.02})_{0.95}Pb(I_{0.98}Br_{0.02})_3$ "98:2 TH" cells at different scan speeds in reverse and forward scan directions for after different ageing times

corresponding to Figure 4b in the main text. The initial and final steady-state (diamond) and ion-freeze PCE (stars) obtained from fast-hysteresis are marked in the degraded measurement.

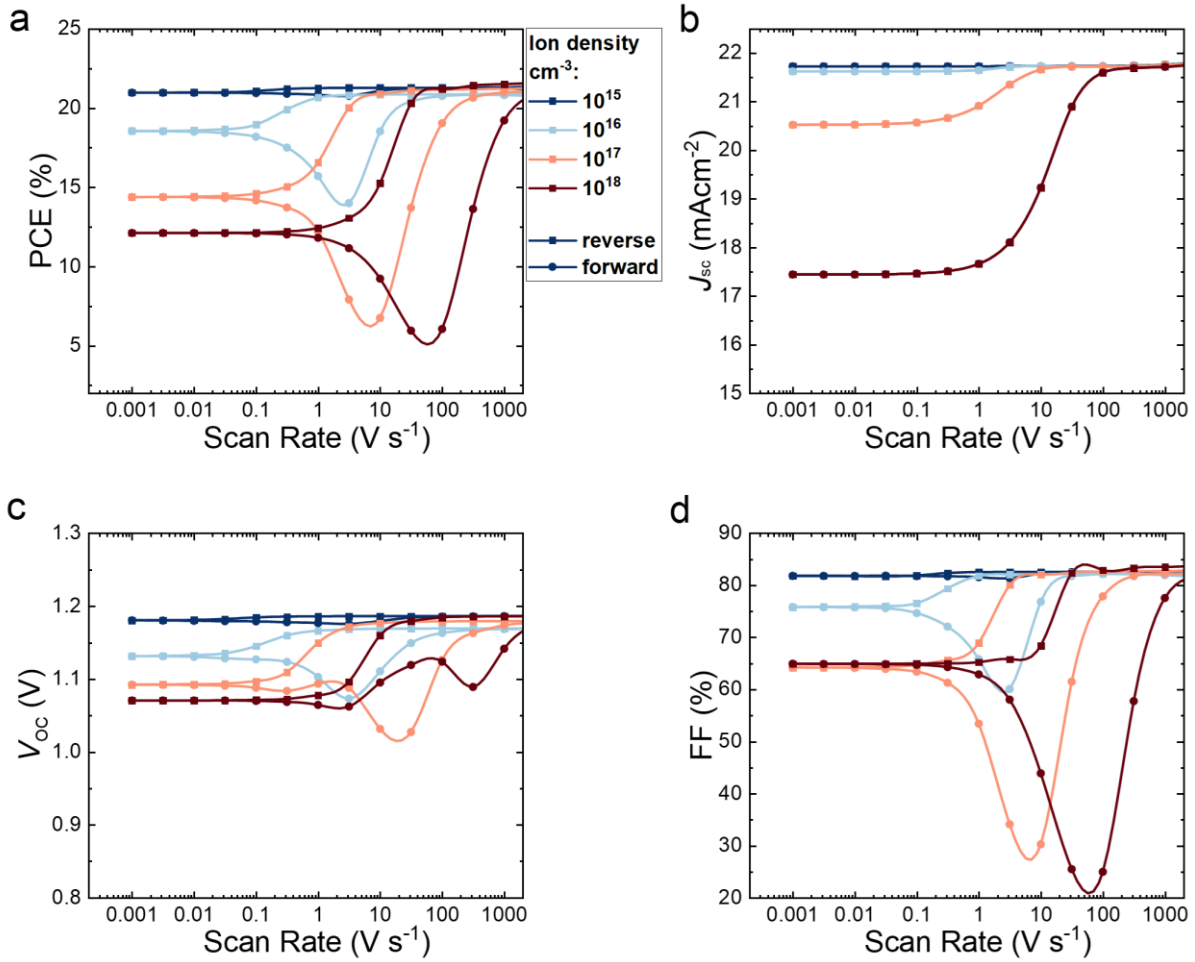

Supplementary Figure 15. Simulated performance metrics PCE (a), J_{SC} (b), V_{OC} (c) and FF (d) for a range of different scan speeds for $Cs_{0.05}(FA_{0.83}MA_{0.17})_{0.95}Pb(I_{0.83}Br_{0.17})_3$ perovskite solar cells with varying mobile ion densities. The prebias was chosen to establish flat band conditions in the perovskite (1.3 V) for a device built-in voltage of 1.5 V. The flat band condition can be identified from the point at which the V_{OC} at fast scan speeds remains unaffected even in the case of large mobile ion densities.

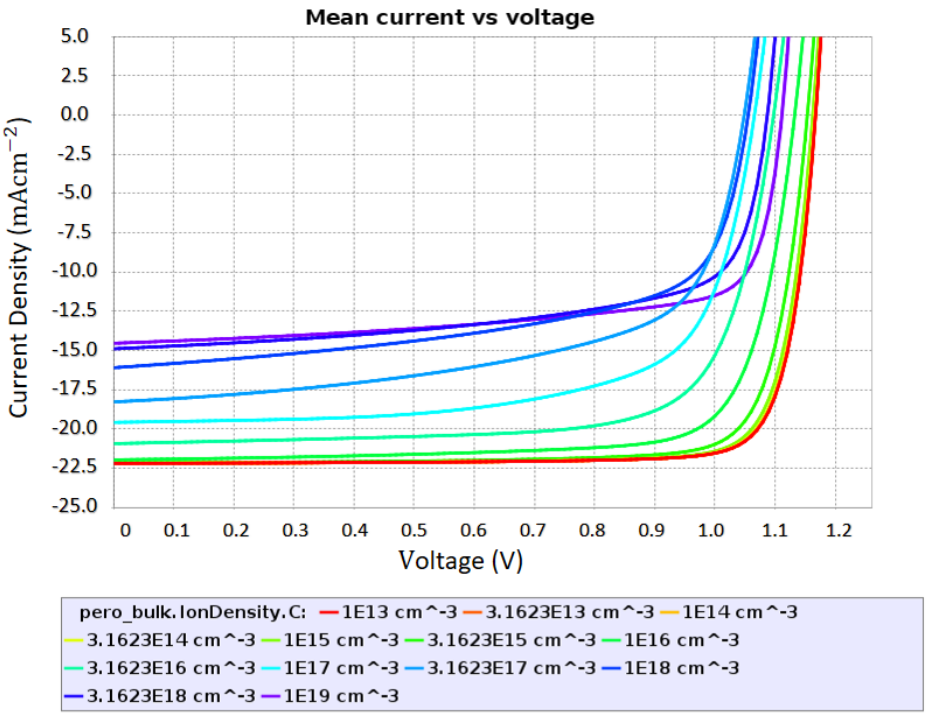

Supplementary Figure 16. Simulated steady-state *JV* curves for $Cs_{0.05}(FA_{0.83}MA_{0.17})_{0.95}Pb(I_{0.83}Br_{0.17})_3$ perovskite solar cells with varying mobile ion densities. It can be seen that increasing mobile ion densities lead to significant current losses once the ion densities pass the threshold of about 10^{15} cm^{-3}.

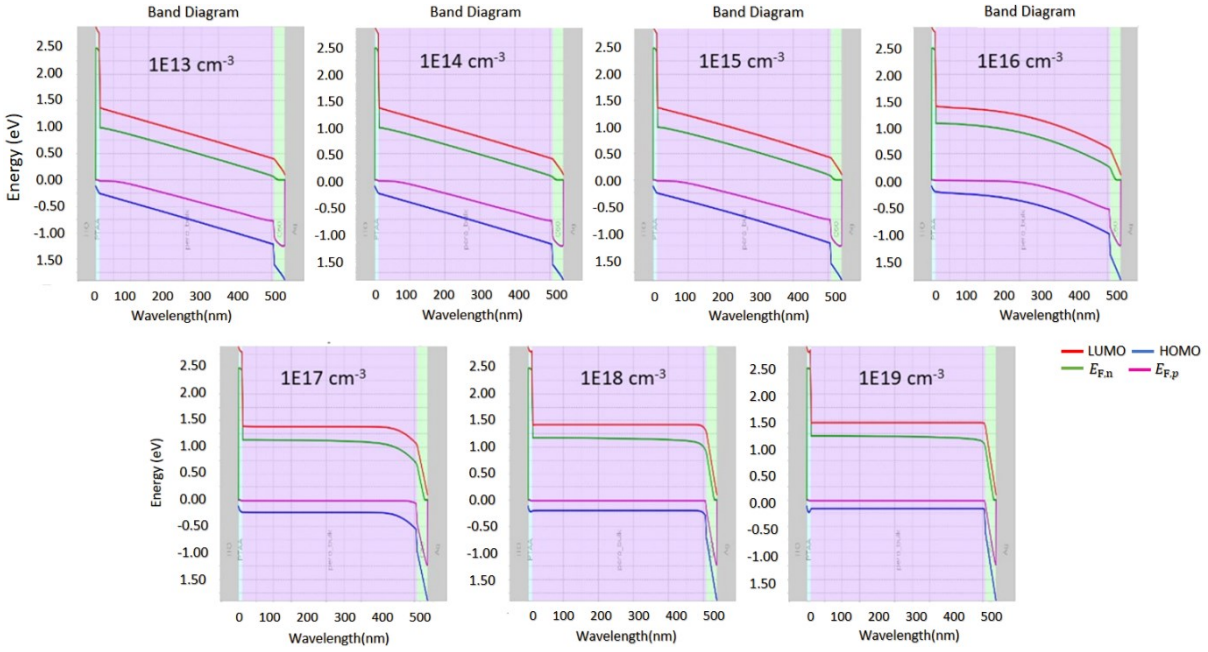

Supplementary Figure 17. Simulated band diagrams at 0V for devices with different mobile ion densities. It can be seen that increasing mobile ion densities lead to significant flattening of the bands, which in turn causes a reduced charge carrier extraction efficiency and leads to the current losses observed in the *JV* curves displayed in Supplementary Figure 16.

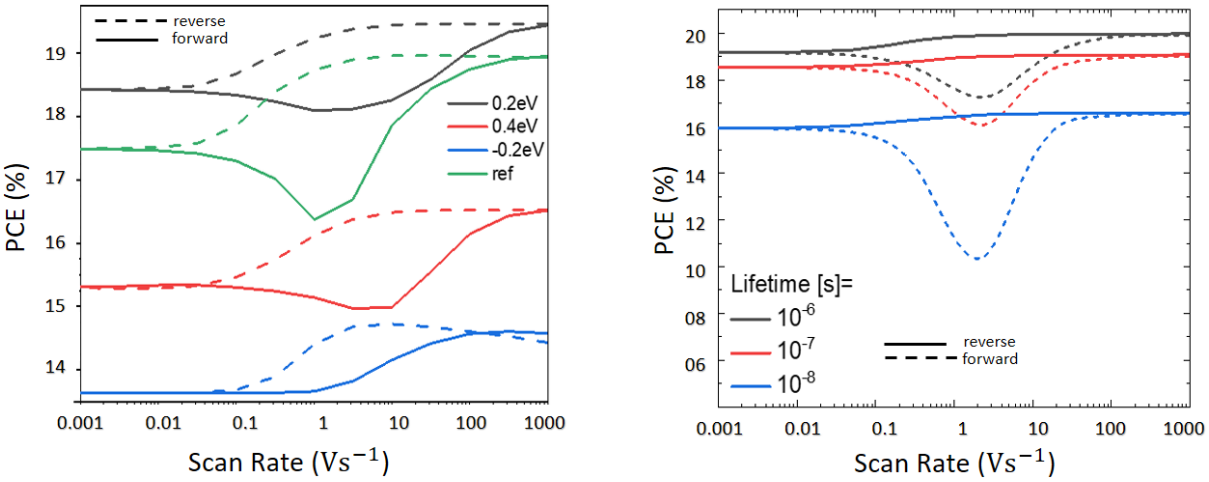

Supplementary Figure 18. Simulated performance metrics PCE for a range of different scan speeds for $Cs_{0.05}(FA_{0.83}MA_{0.17})_{0.95}Pb(I_{0.83}Br_{0.17})_3$ perovskite solar cells with varying interfacial energy offsets and **b** bulk lifetimes.

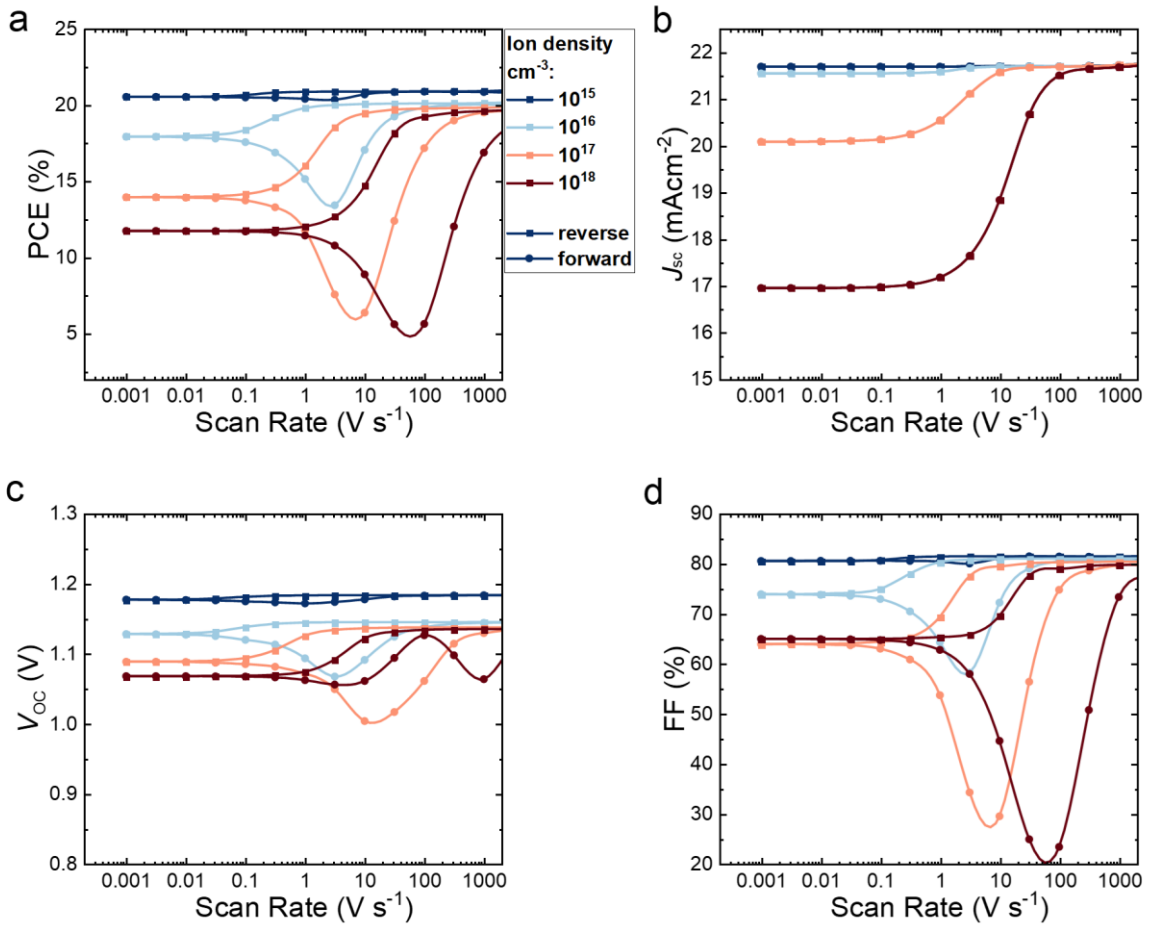

Supplementary Figure 19. Simulated performance metrics PCE (**a**), J_{SC} (**b**), V_{OC} (**c**) and FF (**d**) for a range of different scan speeds for $Cs_{0.05}(FA_{0.83}MA_{0.17})_{0.95}Pb(I_{0.83}Br_{0.17})_3$ perovskite solar cells with varying mobile ion densities. The prebias was chosen to match the initial V_{OC} (1.18 V) for a device with a built-in voltage of 1.5 V.

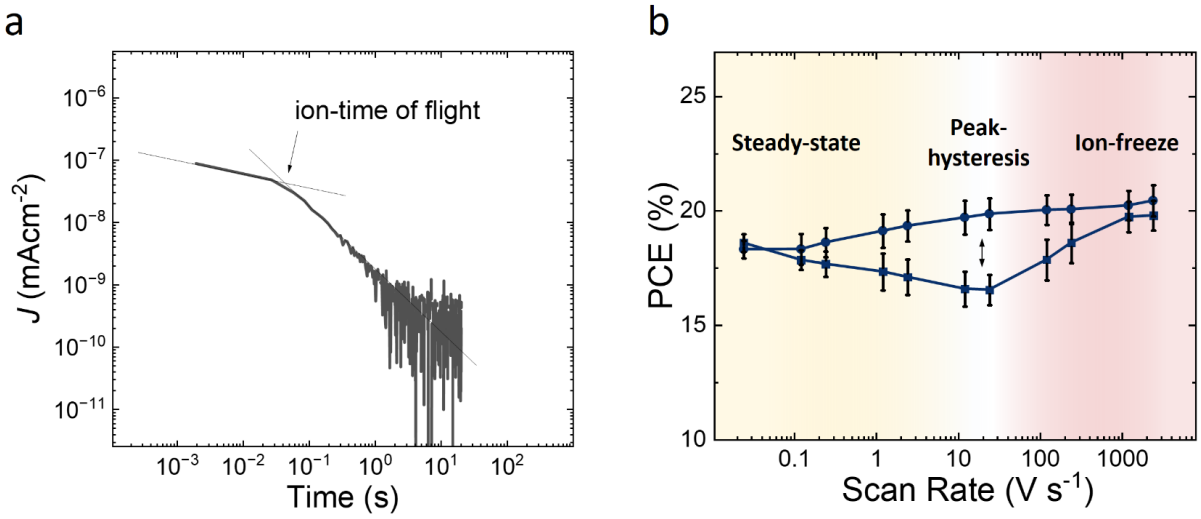

Supplementary Figure 20. a Ion-time of flight transient in a charge extraction experiment (BACE) and **b** scan-rate dependent PCE measured on a fresh $Cs_{0.05}(FA_{0.83}MA_{0.17})_{0.95}Pb(I_{0.83}Br_{0.17})_3$ perovskite solar cell with increased time resolution. The efficient transit time of the mobile ions is ~50 ms matches the peak hysteresis in averaged FH measurements on 5 fresh devices (50 ms scan time). The associated effective ion mobility is μ = 2x10^{-8} cm^2/Vs and the diffusion coefficient D = 7x10^{-10} cm/s. The thin solid lines in are a guide to the eye of the transient behaviour before and after carrier arrival at the electrodes. Data in panel b are presented as mean values +/- SD.

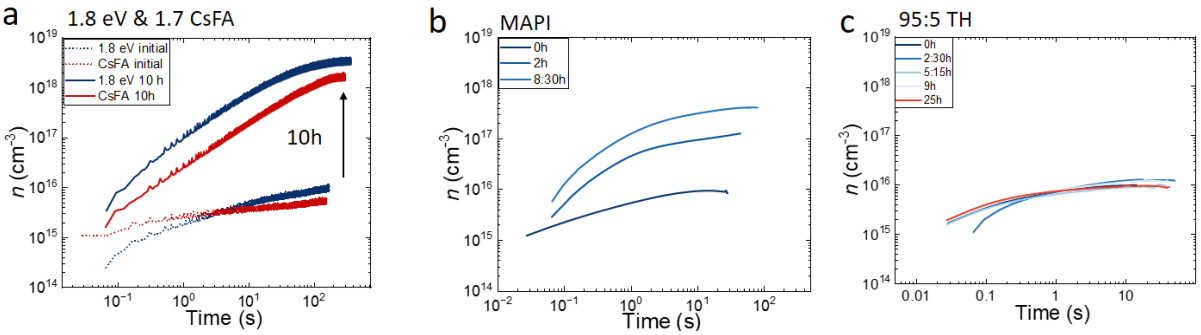

Supplementary Figure 21. Bias Assisted Charge Extraction (BACE) measurements for **a** 1.8 eV WG ($Cs_{0.05}(FA_{0.6}MA_{0.4})_{0.95}Pb(I_{0.6}Br_{0.4})_3$) and CsFA ($FA_{0.85}Cs_{0.15}Pb(I_{0.77}Br_{0.23})_3$), **b** $MAPbI_3$, and **c** 95:5 triple halide ($Cs_{0.05}(FA_{0.95}MA_{0.05})_{0.95}Pb(I_{0.95}Br_{0.05})_3$ + 20 mol% MACl) perovskite solar cells after different ageing times. The 95:5 triple halide cells do not show ionic losses (Supplementary Figure 7) and increased ionic densities on these timescales.

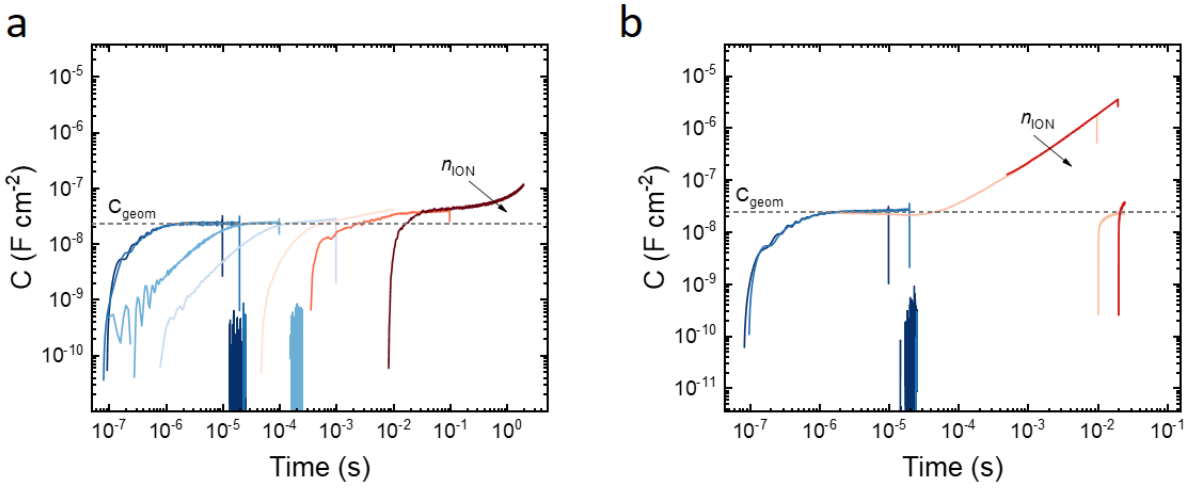

Supplementary Figure 22. Charge Extraction by Linearly Increasing Voltage (CELIV) measurements on **a** fresh and **b** 8-hour aged $Cs_{0.05}(FA_{0.83}MA_{0.17})_{0.95}Pb(I_{0.83}Br_{0.17})_3$ perovskite solar cells revealing a huge increase of the capacitance (as calculated from $C = V/(SR_{\mathrm{Load}})$, where V is recorded voltage on the oscilloscope, S slope of the applied voltage pulse and R_{Load} the load resistance) at long timescales on the aged device.

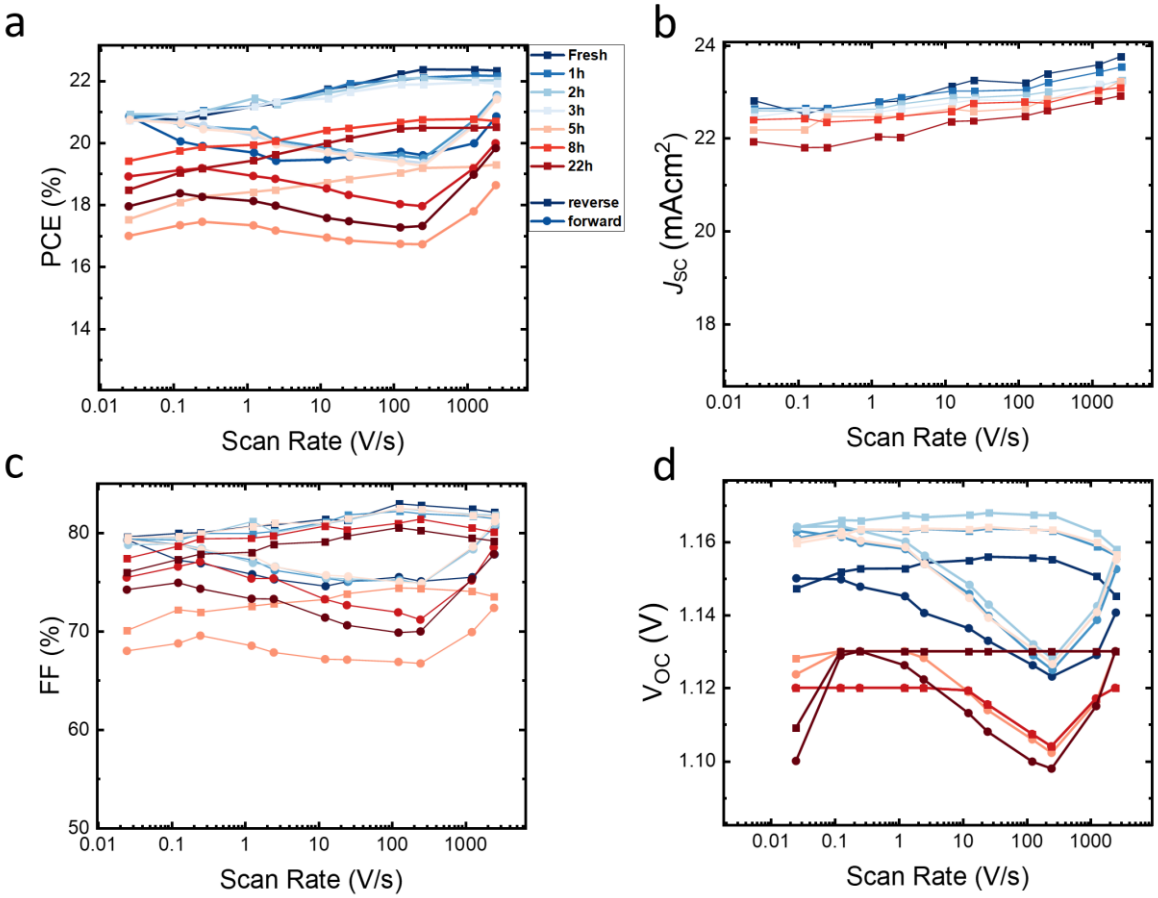

Supplementary Figure 23. a The power conversion efficiency (PCE), **b** short-circuit current density (J_{SC}), **c** open-circuit voltage (V_{OC}), and **d** fill factor (FF) measured at different scan speeds for

$Cs_{0.05}(FA_{0.83}MA_{0.17})_{0.95}Pb(I_{0.83}Br_{0.17})_3$ perovskite solar cells after different ageing times. Ageing was carried out by keeping the cell at 75 °C in the dark. We note the measurement at 5 h is an outlier.

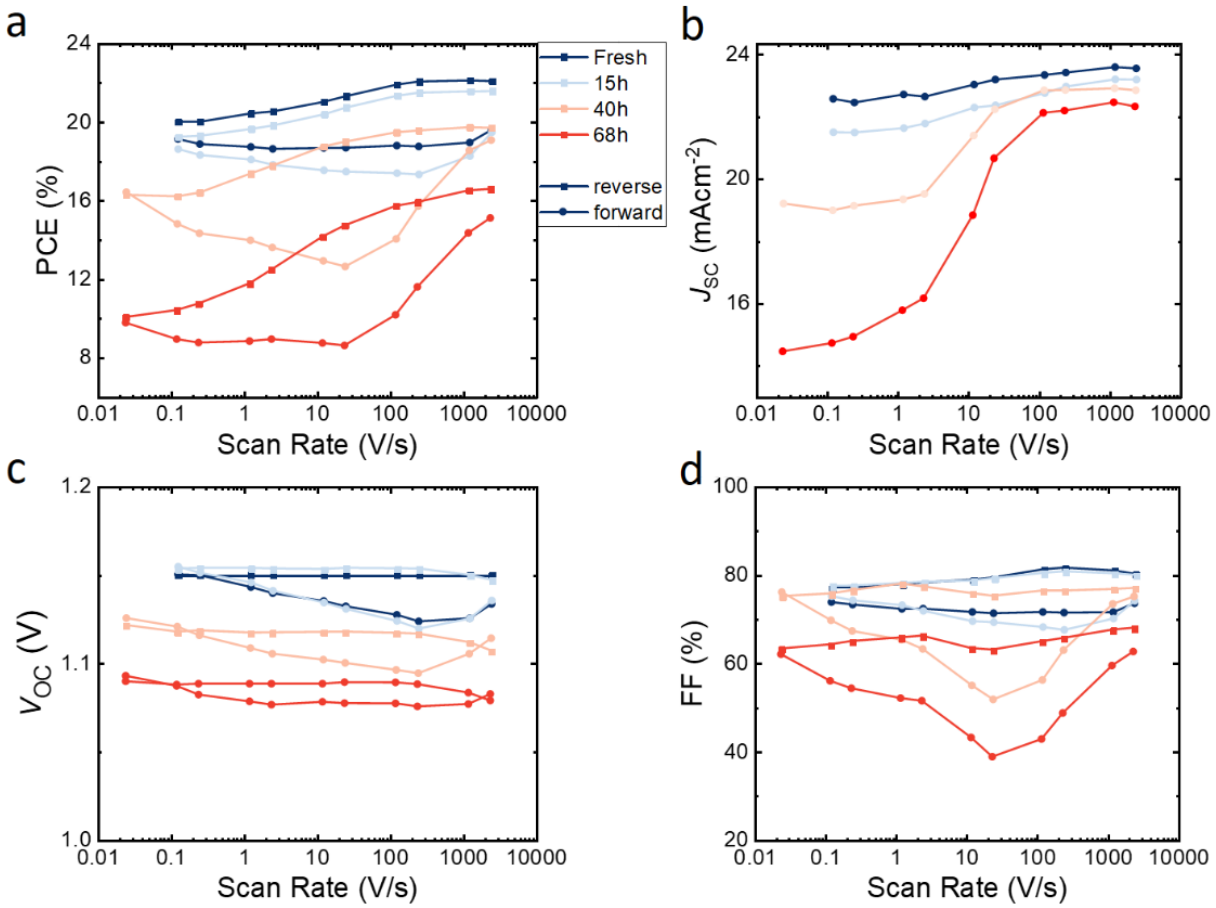

Supplementary Figure 24. a The power conversion efficiency (PCE), **b** short-circuit current density (J_{SC}), **c** open-circuit voltage (V_{OC}), and **d** fill factor (FF) measured at different scan speeds for $Cs_{0.05}(FA_{0.83}MA_{0.17})_{0.95}Pb(I_{0.83}Br_{0.17})_3$ perovskite solar cells after different ageing times. Ageing was carried out at MPP conditions under 1 sun equivalent illumination with a white LED in a glovebox.

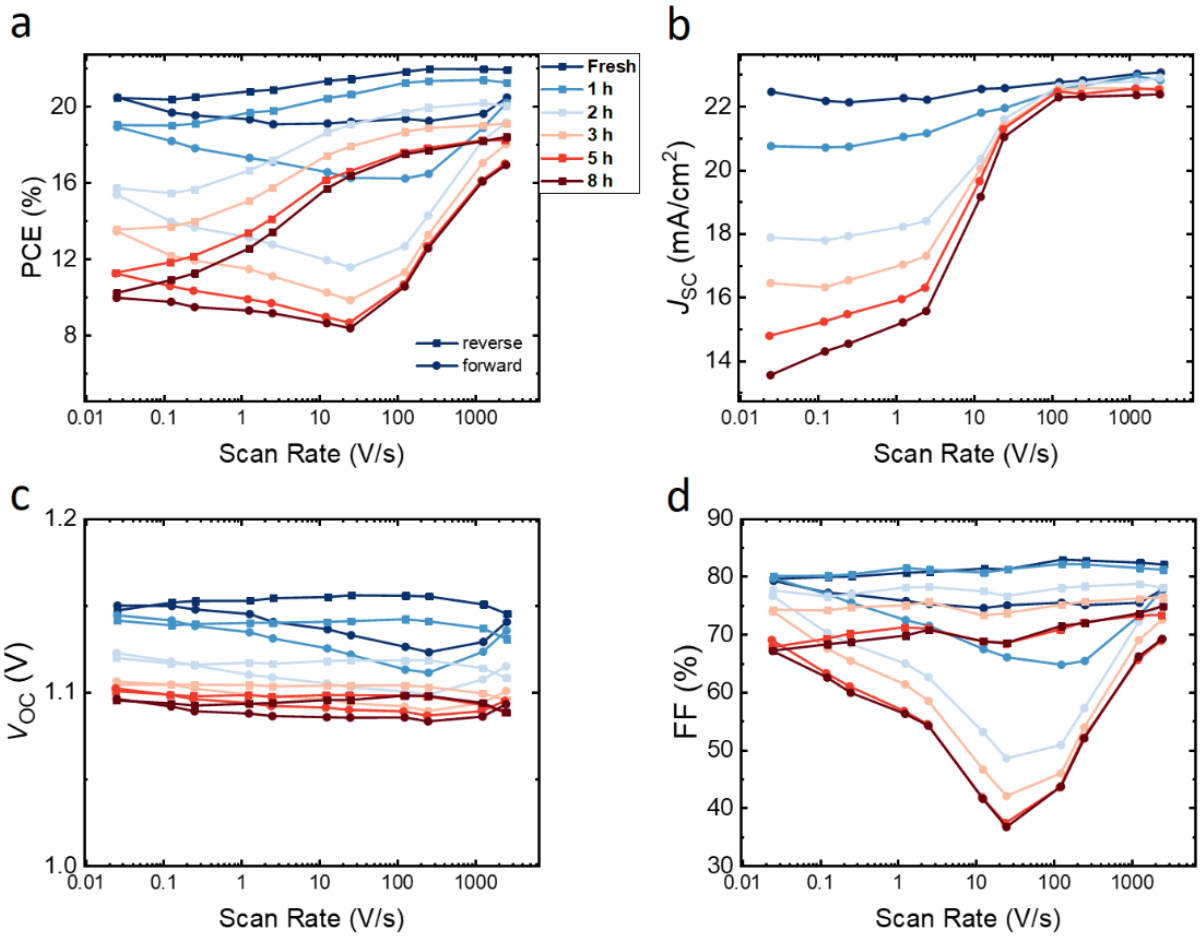

Supplementary Figure 25. a The power conversion efficiency (PCE), **b** short-circuit current density (J_{SC}), **c** open-circuit voltage (V_{OC}), and **d** fill factor (FF) measured at different scan speeds for $Cs_{0.05}(FA_{0.83}MA_{0.17})_{0.95}Pb(I_{0.83}Br_{0.17})_3$ perovskite solar cells after different ageing times. Ageing was carried out by keeping the device in the dark and in the glovebox and applying a forward bias to it to inject the J_{SC} of the cell.

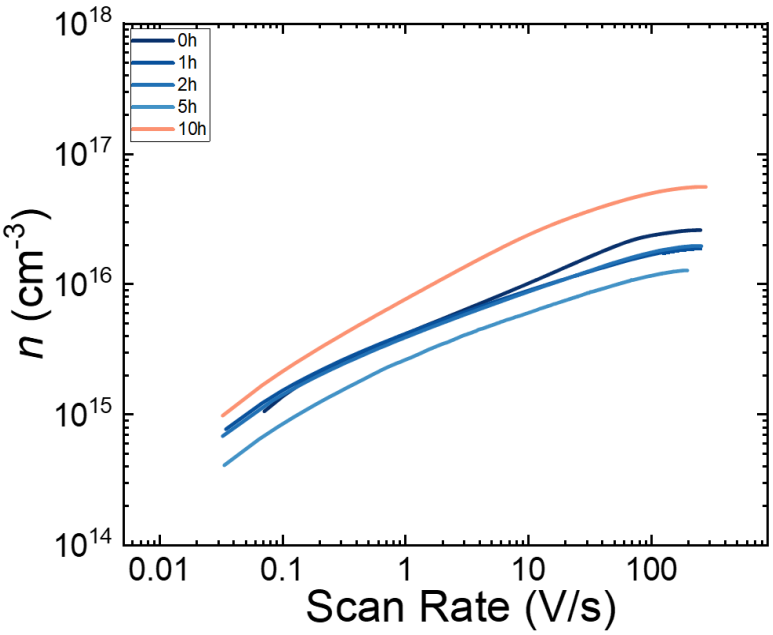

Supplementary Figure 26. Bias Assisted Charge Extraction (BACE) measurements for $Cs_{0.05}(FA_{0.83}MA_{0.17})_{0.95}Pb(I_{0.83}Br_{0.17})_3$ perovskite solar cells by keeping the cell at 85 °C for the specified time.

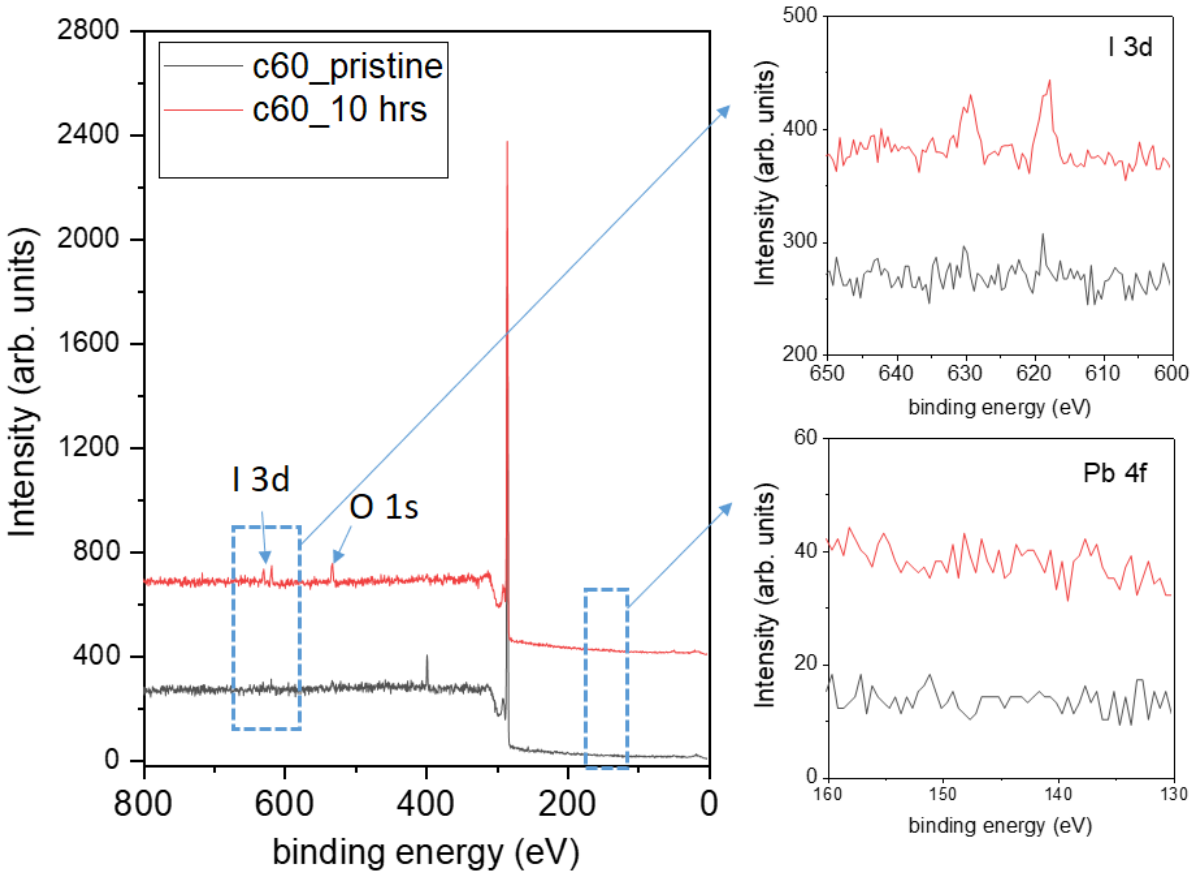

Supplementary Figure 27. XPS survey of Si wafers suspended (distance of ca. 1 mm) on top of different perovskite films (the neat TC films, TC capped with C_{60} and TC capped with C60 and 1 nm (100 nm) of

Cu) after 10 hours of illumination. We observe the capture of iodine for the bare perovskite sample, evidencing the release of iodine under illumination but no other perovskite species (e.g., iodine or lead) for all other sample stacks suggesting an effective diffusion barrier on these short timescales.

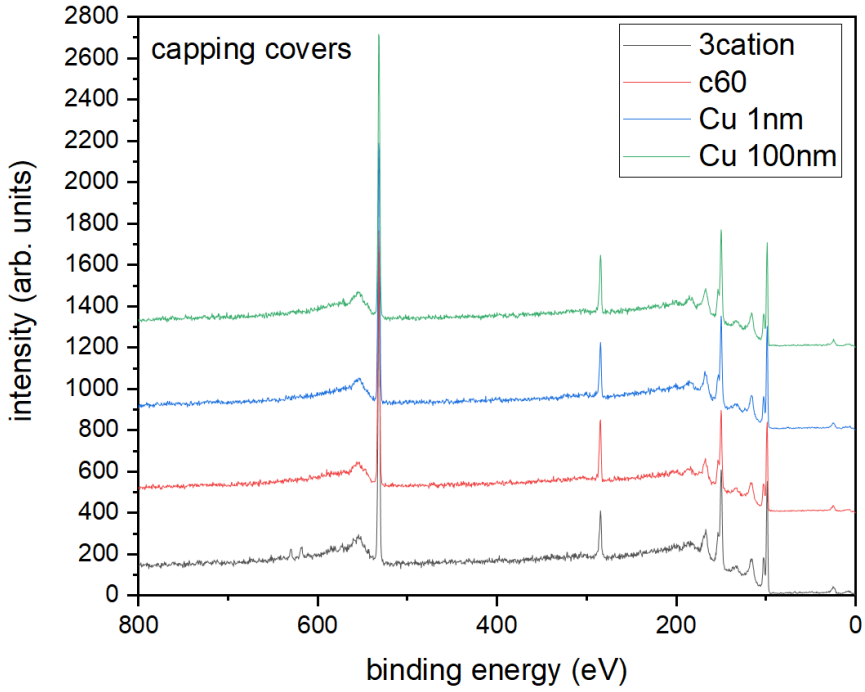

Supplementary Figure 28. An XPS survey of Si wafers suspended on top (at a distance of ca. 1 mm) of different perovskite films, i.e. the neat 83-17 triple cation (TC) film, TC capped with C_{60} and TC capped with C_{60} and 1 nm (100 nm) of Cu, after 10 hours of illumination. We observe the capture of iodine for the bare perovskite sample, evidencing the release of iodine under illumination but no other perovskite species (e.g., iodine or lead) for all other sample stacks suggesting an effective diffusion barrier on these short timescales.

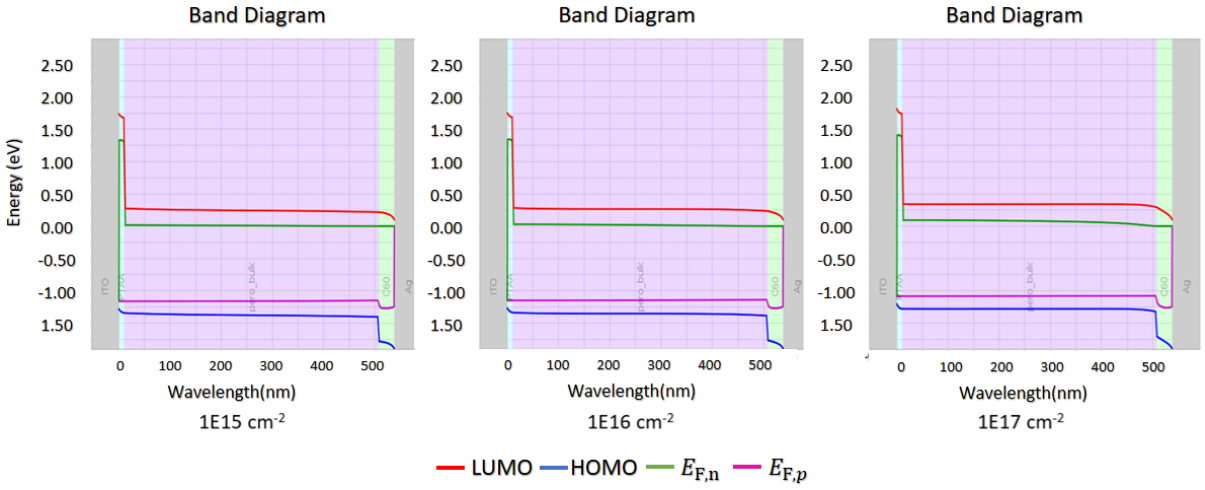

Supplementary Figure 29. Simulated band diagrams at V_{OC} for devices with a V_{BI} of 1.5 V with different mobile ion densities. It can be seen that increasing mobile ion densities lead to a stronger QFLS bending closer to the perovskite – C_{60} interface. The QFLS in the bulk remains nearly constant (1.167 eV, 1.162,

and 1.154 eV) for mobile ion densities of 10^{15}, $10^{16,}$ and 10^{17} cm^{-3} respectively. However, despite the near-constant QFLS, the V_{OC} of the simulated *JV* curves is strongly reduced with increasing ion densities, dropping from 1.165 through 1.140 to 1.077 V. The origin of this effect is discussed in Supplementary Figure 30.

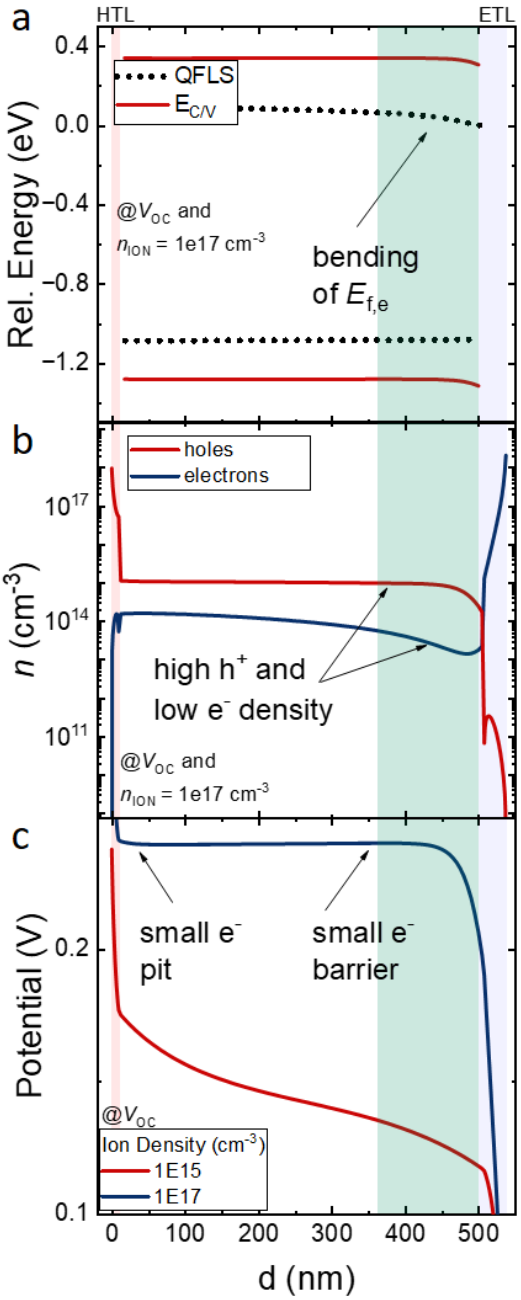

Supplementary Figure 30. a The band diagram showing the conduction and valence band as well as electron and hole quasi-Fermi levels (QFLs) for a device with a V_{BI} of 1.5 V at its V_{OC} (1.14) reveals a bending of the electron QFL at the C_{60} interface. **b** The carrier density profile at V_{OC} shows an excess of holes in the device, while the electron density drops in the vicinity to the C_{60} layer. This is due to the screened internal field in case of a higher ion density which is shown in panel **c.** Considering that the total (electron and hole) current depends on the conductivity and the gradient of the QFL, i.e. $J_{\mathrm{e/h}} = \sigma_{\mathrm{e,h}}/e \ * \nabla E_{\mathrm{f,e/h}}$ and that the electron and hole current have to be equal at V_{OC}, follows that: $\frac{\sigma_h}{\sigma_e} = \frac{\nabla E_{\mathrm{f,e}}}{\nabla E_{\mathrm{f,h}}} \rightarrow \nabla E_{\mathrm{f,e}} = \frac{\sigma_h}{\sigma_e} \cdot \nabla E_{\mathrm{f,h}}$.[1–3] Because the conductivity of holes is greatly enhanced at the electron-

selective interface, while the electron conductive is strongly decreased (inversion population), allows us to conclude that the electron QFL bends at the C_{60} interface.

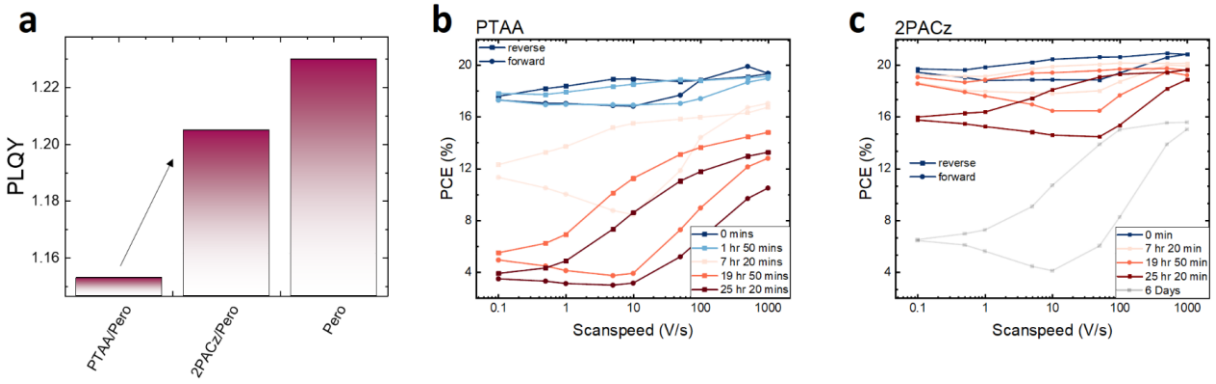

Supplementary Figure 31. **a** Comparison of photoluminescence quantum yield of PTAA/perovskite and 2PACz/perovskite and the neat perovskite on quartz. Scan rate-dependent PCE of triple cation perovskite on **b** PTAA and **c** SAM as well as PLQY data highlighting the Improvement through 2PACz.

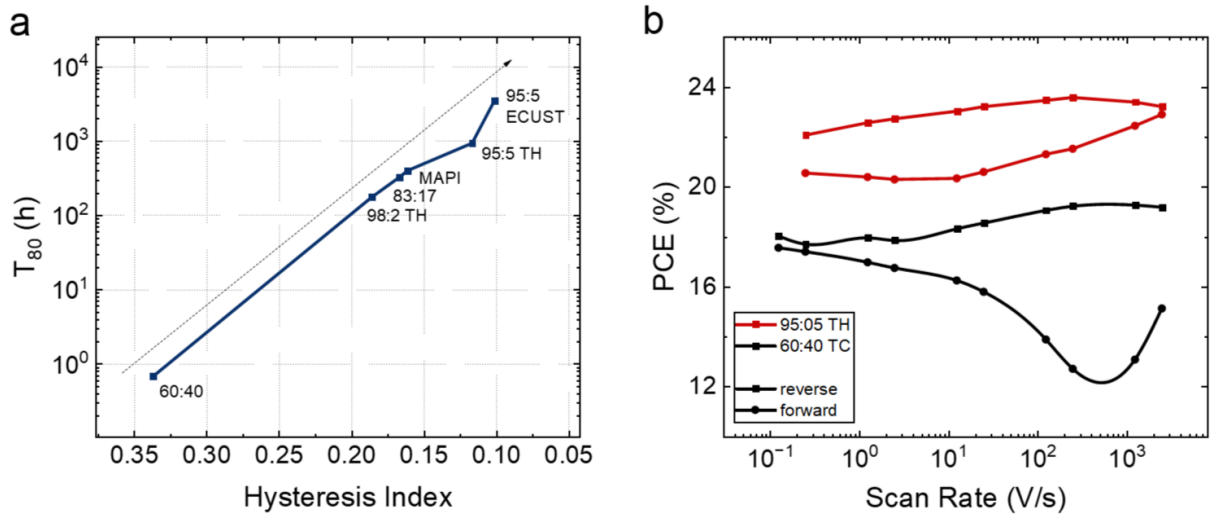

Supplementary Figure 32. a T80 stability versus hysteresis index (HI = 1 – PCE_{fwd}/PCE_{rev}). The graph highlights a correlation between the stability under maximum power point tracking at 1 sun illumination and the HI based on the data points available so far. **b** Exemplifies the scan rate-dependent efficiency for the 95:5 TH (FAPI-rich) and the least stable 60:40 (MAPbBr-rich) device with a larger hysteresis in the latter. Interestingly, if the hysteresis were measured at a scan speed typically used e.g. at 100 mV/s, the MAPbBr-rich would appear to have a lower hysteresis. This highlights the importance of assessing the full extent of the hysteresis based on the scan rate-dependent measurements.

Supplementary Table S1. IonMonger simulation parameters for the 83:17 triple cation standard cell.

Parameter	Symbol	Value	Unit	Ref.
Majority carrier band offset between perovskite and C_{60}	$\Delta E_{\mathrm{maj,c}}$	0	eV	[4]
Majority carrier band offset between perovskite and PTAA	$\Delta E_{\mathrm{maj,v}}$	0	eV	[4]
Lifetime in perovskite	τ_{pero}	200	ns	[5]
Ionized acceptors in PTAA	$N_{\mathrm{A},p}^{-}$	0	cm^{-3}	
Ionized donors in C_{60}	$N_{\mathrm{D},n}^{+}$	0	cm^{-3}	
Minority carrier recombination velocity from perovskite to PTAA	$S_{\mathrm{min},n}$	500	cm/s	[5]
Minority carrier recombination velocity from perovskite to C_{60}	$S_{\mathrm{min},p}$	2000	cm/s	[5]
Thickness of PTAA	d_{PTAA}	10	nm	
Thickness of perovskite	d_{pero}	400	nm	
Thickness of C_{60}	d_{C60}	30	nm	
Offset between metal and PTAA	$\Delta E_{\mathrm{F,metal-}}$	0.05	eV	
Offset between metal and C_{60}	$\Delta E_{\mathrm{F,metal-}}$	0.05	eV	
Device built-in voltage	V_{BI}	1.5	V	
Bandgap PTAA	$E_{\mathrm{G,PTAA}}$	3.0	eV	
Electron affinity PTAA	$E_{\mathrm{A,PTAA}}$	2.5	eV	
Bandgap perovskite	$E_{\mathrm{G,pero}}$	1.63	eV	
Electron affinity perovskite	$E_{\mathrm{A,pero}}$	3.9	eV	[4]
Electron affinity C_{60}	$E_{\mathrm{A,C60}}$	3.9	eV	
Bandgap C_{60}	$E_{\mathrm{G,C60}}$	2.0	eV	
Electron mobility in C_{60}	$\mu_{n,\mathrm{C60}}$	$1x10^{-2}$	cm^2/Vs	[6]
Hole mobility in PTAA	$\mu_{p,\mathrm{PTAA}}$	$1x10^{-4}$	cm^2/Vs	[7]
Electron mobility in perovskite	$\mu_{n,\mathrm{pero}}$	1	cm^2/Vs	
Hole mobility in perovskite	$\mu_{p,\mathrm{pero}}$	1	cm^2/Vs	
Relative dielectric constant PTAA	ϵ_{PTAA}	3.5		[8]
Relative dielectric constant perovskite	ϵ_{pero}	22		[9]
relative dielectric constant C_{60}	ϵ_{C60}	5.0		[10]
Effective electron density of states in HTL	$N_{\mathrm{C/V,PTAA}}$	$1x10^{20}$	cm^{-3}	[11]
Effective electron density of states in C_{60}	$N_{\mathrm{C/V,C60}}$	$1x10^{20}$	cm^{-3}	[11]
Effective electron density of states in perovskite	$N_{\mathrm{C/V,pero}}$	$2.2x10^{18}$	cm^{-3}	[12]
Effective ion density	N_{ion}	variable	cm^{-3}	
Effective ion diffusion constant	D_{ion}	$5x10^{-10}$	cm^2/s	

Supplementary Note 1 - Understanding of losses at fast-scan speeds

It should be noted that the presence of mobile ions can still affect the PCE even when they are immobilized depending on their distribution and accumulation throughout the device and at the interfaces during the prebias.[13,14] As discussed in the main text a QFLS-eV_{OC} mismatch is observed in various systems, which we believe is likely due to ions accumulation in an unfavorable position under open-circuit conditions or the prebias of the FH measurement (e.g. cations at the hole selective interface).[52] The QFLS-eV_{OC} mismatch occurs in all studied systems and leads to a parallel downward shift of the V_{OC} as a function of scan speed with aging time. Therefore, we attribute part of the PCE loss at fast-scan speeds to an ionic loss. An example of this scenario is shown in **Supplementary Figure 19**, which demonstrates a drop in V_{OC} that is largely independent of scan speed. However, it can be also seen that ion accumulation at the interfaces would still lead to a nearly unchanged FF at the highest scan speeds. Therefore, we believe that the devices shown in **Supplementary Figure 4** - **Supplementary Figure 6** (60:40, CsFA and MAPI) are affected by non-ionic charge transport losses that affect the FF at fast-scan speeds. For the 83-17 triple cation, the losses at fast-scan speeds (especially those that cannot be attributed to a QFLS-V_{OC} are very small, see grey area **Figure 7a**), hence these losses are not that critical. Overall, while we focus here on the losses from fast-to-slow scan speeds, more experimental and numerical work is necessary to better understand the losses at fast-scan speeds.

Supplementary Note 2 - Understanding the timescales in fast hysteresis and bias-assisted charge extraction

The FH simulations in **Figure 5a** did not consider a change in the mobility of the mobile ions, just an increase in the carrier density. Yet, the timescale of the peak hysteresis is getting shorter with an increasing ion density. This makes sense, as at ion densities above the *CU* charge, the internal field becomes more and more screened which reduces the depletion width. Thus, the drift distance of ions becomes shorter, and therefore, their response time. In contrast, in the experiment, this is not observed, in fact, in a majority of cases, the response becomes slower (i.e. the peak hysteresis shifts to longer timescales). This is most dominant in the case of the 60:40, and the 83:17 triple cation, less so in MAPI (although visible at longer aging times), and basically completely absent in the CsFA device. This is consistent with BACE measurements (**Figure 6a**), which revealed a substantial slowdown of charge extraction. As for FH, this would not be expected in the case of constant ion mobility, as once the ion density exceeds the *CU* charge ($\approx 10^{16}$ cm^{-3}), the drift time of ions gets shorter due to enhanced field screening and shorter depletion width.

Therefore, we believe that either mobile ions get slower due to some reason, or that another ionic species takes over (e.g. MA vacancies considering the clear absence of the slowdown in CsFA). However, it has been previously observed, that ion migration proceeds via the grain boundaries and volume transport in less stable compositions. Grain boundary diffusion is up to 2 orders of magnitude faster than volume diffusion.[15] This could explain the considerable slow-down of ionic motion and is consistent with this previous work as it highlights that once volume diffusion occurs the devices get less stable.[15] However, we also note that the less stable device, i.e. the 60:40 triple cation has a very fast initial response in the FH (**Supplementary Figure 6**). Clearly, further research is required to fully understand this intriguing change in timescales.

Supplementary References:

1. Onno, A., Chen, C. & Holman, Z. C. Electron and hole partial specific resistances: A framework to understand contacts to solar cells. *Conf. Rec. IEEE Photovolt. Spec. Conf.* 2329–2333 (2019)

doi:10.1109/PVSC40753.2019.8980762.

2. Würfel, P. & Würfel, U. *Physics of Solar Cells: From Basic Principles to Advanced Concepts*. (Wiley-VCH, 2009).

3. Kavadiya, S. *et al.* Investigation of the Selectivity of Carrier Transport Layers in Wide-Bandgap Perovskite Solar Cells. *Sol. RRL* **5**, 1–9 (2021).

4. Stolterfoht, M. *et al.* The impact of energy alignment and interfacial recombination on the internal and external open-circuit voltage of perovskite solar cells. *Energy Environ. Sci.* **12**, 2778–2788 (2019).

5. Stolterfoht, M. *et al.* Visualization and suppression of interfacial recombination for high-efficiency large-area pin perovskite solar cells. *Nat. Energy* **3**, 847–854 (2018).

6. Mendil, N., Daoudi, M., Berkai, Z. & Belghachi, A. Disorder effect on carrier mobility in Fullerene organic semiconductor. *J. Phys. Conf. Ser.* **647**, 012057 (2015).

7. Luo, J. *et al.* Toward high-efficiency, hysteresis-less, stable perovskite solar cells: Unusual doping of a hole-transporting material using a fluorine-containing hydrophobic Lewis acid. *Energy Environ. Sci.* **11**, 2035–2045 (2018).

8. Torabi, S. *et al.* Strategy for enhancing the dielectric constant of organic semiconductors without sacrificing charge carrier mobility and solubility. *Adv. Funct. Mater.* **25**, 150–157 (2015).

9. Brivio, F., Butler, K. T., Walsh, A. & Van Schilfgaarde, M. Relativistic quasiparticle self-consistent electronic structure of hybrid halide perovskite photovoltaic absorbers. *Phys. Rev. B - Condens. Matter Mater. Phys.* **89**, 1–6 (2014).

10. Chern, G., Mathias, H., Testardi, L. R., Seger, L. & Schlenoff, J. Low-frequency dielectric permittivity of C60. *J. Supercond.* **8**, 207–210 (1995).

11. Kirchartz, T. *et al.* Sensitivity of the Mott–Schottky analysis in organic solar cells. *J. Phys. Chem. C* **116**, 7672–7680 (2012).

12. Staub, F. *et al.* Beyond Bulk Lifetimes: Insights into Lead Halide Perovskite Films from Time-Resolved Photoluminescence. *Phys. Rev. Appl.* **6**, 044017 (2016).

13. Le Corre, V. M. *et al.* Quantification of Efficiency Losses Due to Mobile Ions in Perovskite Solar Cells via Fast Hysteresis Measurements. *Sol. RRL* **6**, 2100772 (2022).

14. Jacobs, D. A. *et al.* Hysteresis phenomena in perovskite solar cells: The many and varied effects of ionic accumulation. *Phys. Chem. Chem. Phys.* **19**, 3094–3103 (2017).

15. Ghasemi, M. *et al.* A multiscale ion diffusion framework sheds light on the diffusion–stability–hysteresis nexus in metal halide perovskites. *Nat. Mater.* **22**, 329–337 (2023).